ARMA 16-0168

Simulation of mode II unconstrained fracture path formation coupled with continuum anisotropic damage propagation in shale

Jin, W. and Arson, C.
Georgia Institute of Technology, Atlanta, GA, USA
Busetti, S.
ConocoPhillips, Houston, TX, USA

ABSTRACT: The objective of this work is to simulate mode II multi-scale fracture propagation in shale by coupling a continuum anisotropic damage model with a Cohesive Zone Model (CZM). The Continuum Damage Mechanics – based Differential Stress Induced Damage (DSID) model is used to represent micro-scale crack evolution. DSID parameters were calibrated against pre-peak points of stress/strain curves obtained experimentally during triaxial compression tests performed in Bakken shale. A bilinear CZM is employed to represent macroscale fracture propagation. We calculated the effective shear modulus of a continuum that contained a distribution of parallel cracks according to the DSID model (which does not account for crack interactions) and according to Kachanov's micromechanical model (which accounts for crack interactions). Simulations confirmed that above a crack density or damage of 0.3, crack interactions could not be ignored, and we used that threshold to define the transition between continuum damage propagation and discrete fracture propagation and subsequently, to calibrate the shear cohesive strength of the CZM. The CZM cohesive energy release rate was determined by calibrating a numerical model of triaxial compression test against experimental data obtained on Bakken shale. The cylindrical sample was modeled with a CZM to pre-define an inclined cohesive fracture, and the DSID model was assigned to the surrounding elements. We used our calibrated CZM-DSID model to simulate a biaxial compression test in plane strain. Results clearly show that the proposed modeling strategy not only allows simulating the advancement of macro-fracture tips, but also captures the inception and growth of micro-cracks that form damaged zones, as well as the transition between smeared damage and discrete fracture.

1. INTRODUCTION

The analysis of fracture propagation in geomaterials (such as rock, concrete) still remains a challenge from the perspective of numerical modeling, which needs to capture micro crack (damage) inception and growth up to the point of macro fracture initiation and propagation, and the formation of fracture paths after the global softening in later simulation stages. State-of-the-Art finite element tools are either based on Continuum Damage Mechanics (CDM) or on Fracture Mechanics (FM). In CDM, fractures are considered as the ultimate stage of damage accumulation, at which the energy dissipated in the damage zone equals the energy that needs to be released to create new surfaces (**Mazars and Pijaudier-Cabot, 1996**). In FM, discontinuous displacement fields propagate through a continuum according to physics-based criteria (**Xu and Needleman, 1994**). FM theories are usually implemented in Cohesive Zone Models (CZM) or Extended Finite Element Methods (XFEM). Because CDM cannot be used to simulate fracture surface debonding at late crack propagation stages and since State-of-the-Art CZM and XFEM do not account for micro-crack propagation prior to fracture surface debonding, several researchers coupled CDM and XFEM (**Comi et al., 2007; Jirasek and Zimmermann, 2001**) or CDM and CZM (**Cuvilliez et al., 2012**). However, even in these coupled models, there is no rigorous calibration of the critical damage threshold that marks the transition between micro-crack propagation and macro-fracture initiation. Moreover, the fracture path depends on the location of the CZ elements or on the interpolation order chosen in the XFEs. Thus in the present study, we propose a numerical method that couples a CDM model (for the bulk) to a Cohesive Zone Model (for the fracture). We present the theoretical framework and calibration method for the CDM model and for the CZM in Sections 2 and 3, respectively. In Section 4, we present the results obtained during simulations of biaxial compression tests in which CZs are placed at the boundaries of all the Finite Elements of the mesh.

2. ANISOTROPIC DAMAGE MODEL

2.1. Theoretical Framework of the DISD model

We study the microscale crack propagation with the DSID model (**Xu and Arson, 2015**). The free enthalpy is expressed in terms of elastic energy and damage induced additional energy, in which the damage variable is defined as a second order tensor $\boldsymbol{\Omega}$ to represent crack evolution inside an REV.

$$G_s(\boldsymbol{\sigma},\boldsymbol{\Omega}) = \frac{1}{2}\boldsymbol{\sigma}:\mathbb{S}_0:\boldsymbol{\sigma} + a_1 \mathrm{Tr}\boldsymbol{\Omega}\left(\mathrm{Tr}\boldsymbol{\sigma}\right)^2 + a_2 \mathrm{Tr}\left(\boldsymbol{\sigma}\cdot\boldsymbol{\sigma}\cdot\boldsymbol{\Omega}\right) + a_3 \mathrm{Tr}\boldsymbol{\sigma}\mathrm{Tr}\left(\boldsymbol{\Omega}\cdot\boldsymbol{\sigma}\right) + a_4 \mathrm{Tr}\boldsymbol{\Omega}\mathrm{Tr}\left(\boldsymbol{\sigma}\cdot\boldsymbol{\sigma}\right) \quad (1)$$

Where a_i are material parameters. $\mathbb{S}_0$ is the reference (undamaged) compliance tensor. The thermodynamic conjugated relationships are the following:

$$\begin{aligned}\boldsymbol{\varepsilon}^E &= \boldsymbol{\varepsilon}^{el} + \boldsymbol{\varepsilon}^{ed} = \boldsymbol{\varepsilon} - \boldsymbol{\varepsilon}^{id} = \frac{\partial G_s}{\partial \boldsymbol{\sigma}} \\ &= \frac{1+\nu_0}{E_0}\boldsymbol{\sigma} - \frac{\nu_0}{E_0}\left(\mathrm{Tr}\boldsymbol{\sigma}\right)\boldsymbol{\delta} + 2a_1\left(\mathrm{Tr}\boldsymbol{\Omega}\mathrm{Tr}\boldsymbol{\sigma}\right)\boldsymbol{\delta} + a_2(\boldsymbol{\sigma}\cdot\boldsymbol{\Omega} \\ &+\boldsymbol{\Omega}\cdot\boldsymbol{\sigma}) + a_3\left[\mathrm{Tr}\left(\boldsymbol{\Omega}\cdot\boldsymbol{\sigma}\right)\boldsymbol{\delta} + \left(\mathrm{Tr}\boldsymbol{\sigma}\right)\boldsymbol{\Omega}\right] + 2a_4\left(\mathrm{Tr}\boldsymbol{\Omega}\right)\boldsymbol{\sigma} \quad (2)\end{aligned}$$

$$\begin{aligned}\mathbf{Y} &= \frac{\partial G_s}{\partial \boldsymbol{\Omega}} = a_1\left(\mathrm{Tr}\boldsymbol{\sigma}\right)^2\boldsymbol{\delta} + a_2\boldsymbol{\sigma}\cdot\boldsymbol{\sigma} \\ &+ a_3\left(\mathrm{Tr}\boldsymbol{\sigma}\right)\boldsymbol{\sigma} + a_4\mathrm{Tr}\left(\boldsymbol{\sigma}\cdot\boldsymbol{\sigma}\right)\boldsymbol{\delta}\end{aligned}$$

In which E_0 and ν_0 are Young's modulus and Poisson ratio of initial undamaged material. As shown in Fig 1, $\boldsymbol{\varepsilon}^{el}$ is the purely elastic strain, $\boldsymbol{\varepsilon}^{ed}$ is the elastic damage-induced strain that result from the degradation of mechanical stiffness, and $\boldsymbol{\varepsilon}^{id}$ is the irreversible strain. The damage criterion is a Drucker Prager yield function expressed in terms of energy release rate instead of stress, which allows predicting the evolution of damage with deviatoric stress:

$$\begin{aligned}f_d &= \sqrt{J^*} - \alpha I^* - k \\ J^* &= \frac{1}{2}\left(\mathbb{P}_1:\mathbf{Y}\text{-}\frac{1}{3}I^*\boldsymbol{\delta}\right):\left(\mathbb{P}_1:\mathbf{Y}\text{-}\frac{1}{3}I^*\boldsymbol{\delta}\right) \quad I^* = \left(\mathbb{P}_1:\mathbf{Y}\right):\boldsymbol{\delta} \\ \mathbb{P}_1(\boldsymbol{\sigma}) &= \sum_{p=1}^{3}\left[H\left(\sigma^p\right) - H\left(-\sigma^p\right)\right]\boldsymbol{n}^p\otimes\boldsymbol{n}^p\otimes\boldsymbol{n}^p\otimes\boldsymbol{n}^p \\ k &= C_0 - C_1\mathrm{Tr}(\boldsymbol{\Omega})\end{aligned} \quad (3)$$

Where C_0 is the initial damage threshold, C_1 is an isotropic hardening variable, $H(\cdot)$ is the Heaviside function, and σ^p is the p-th principal stress. In order to satisfy Clausius-Duhem inequality, the damage potential is defined as:

$$\begin{aligned}g_d &= \sqrt{\frac{1}{2}\left(\mathbb{P}_2:\mathbf{Y}\right):\left(\mathbb{P}_2:\mathbf{Y}\right)} \\ \mathbb{P}_2(\boldsymbol{\sigma}) &= \sum_{p=1}^{3} H\left[\max_{q=1}^{3}\left(\sigma^p\right) - \sigma^p\right]\boldsymbol{n}^p\otimes\boldsymbol{n}^p\otimes\boldsymbol{n}^p\otimes\boldsymbol{n}^p\end{aligned} \quad (4)$$

The flow rule is associated for the irreversible damage strain, and non-associated for damage, as follows:

$$\begin{aligned}\dot{\boldsymbol{\varepsilon}}^{id} &= \dot{\boldsymbol{\lambda}}_d\frac{\partial f_d}{\partial \boldsymbol{\sigma}} = \dot{\boldsymbol{\lambda}}_d\frac{\partial f_d}{\partial \mathbf{Y}}:\frac{\partial \mathbf{Y}}{\partial \boldsymbol{\sigma}} \\ \dot{\boldsymbol{\Omega}} &= \dot{\boldsymbol{\lambda}}_d\frac{\partial g_d}{\partial \mathbf{Y}}\end{aligned} \quad (5)$$

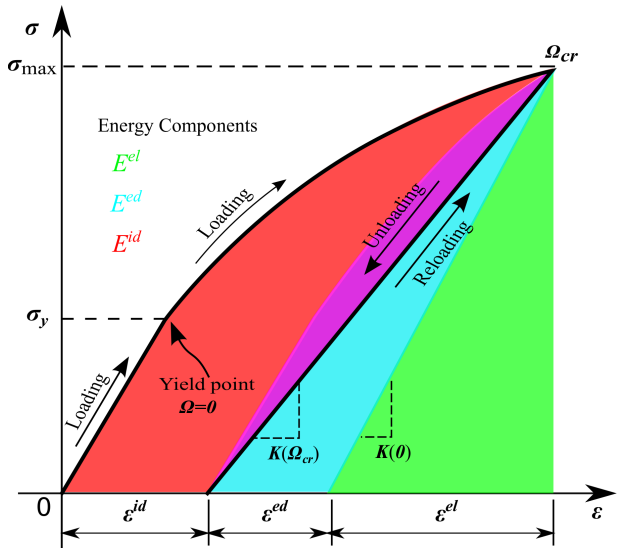

Fig. 1. Energy components in the DSID model

Table 1. Calibrated DSID parameters

Parameters	Units	Value
E_0	*GPa*	46
ν_0	-	0.186
a_1	MPa^{-1}	7.35×10^{-7}
a_2	MPa^{-1}	1.21×10^{-4}
a_3	MPa^{-1}	-3.15×10^{-5}
a_4	MPa^{-1}	2.39×10^{-6}
C_0	*MPa*	0.01
C_1	*MPa*	1.18
α	-	0.399

2.2. Calibration of the DISD model

We calibrated the DSID model against experimental stress/strain curves obtained during triaxial compression tests performed on Bakken shale samples. We used ConocoPhillips rock mechanics dataset (**Amendt et al., 2013**). A dedicated MATLAB code employing the Interior Point Algorithm was adopted to minimize the residual between experimental results y_i and numerical predictions $f(\boldsymbol{x},\boldsymbol{B})$.

$$\begin{aligned}S(\boldsymbol{B}) &= \sum_{i=1}^{n}\left[y_i - f(\boldsymbol{x},\boldsymbol{B})\right]^2 \\ \boldsymbol{B}_{k+1} &= \boldsymbol{B}_k - \gamma_k \mathrm{d}S(\boldsymbol{B}_k)\end{aligned} \quad (6)$$

Where **x** stands for the vector of known input stress increments, and $\boldsymbol{B}$ is the vector of unknown parameters, which needs to be calibrated. At each iteration, the gradient of merit function $S(\boldsymbol{B})$ with respect to each parameter listed in vector $\boldsymbol{B}$ is iteratively calculated. The Barrier penalty parameter γ_k is updated at each time step. The results of the calibration for North Dakota Bakken shale are reported in Table 1.

3. COHESIVE ZONE MODEL

3.1. Bilinear Cohesive Law

Micro-crack interaction is not accounted for in the DSID model, which is not acceptable to model micro-crack propagation after coalescence, which we represent with a Cohesive Zone Model when damage exceeds a critical value Ω_{cr}. Once the damage value inside the DSID elements reaches Ω_{cr}, cohesive elements are activated. According to the traction-separation law used in the CZM, a fracture starts opening, surrounding Finite Elements are unloaded, and damage (micro cracks) stops growing. In the following, we explain how we calibrated the CZM parameters so that the DSID model and the CZM both represent the same rock.

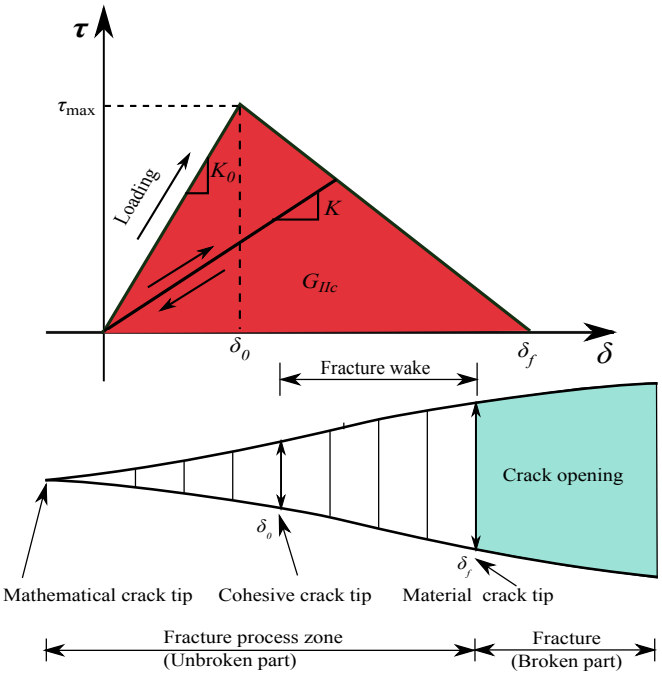

Fig. 2. Bilinear cohesive zone model for pure mode II fracture propagation problems.

For simplicity, we chose a bilinear CZM (Figure 2) to model macro fracture propagation in North Dakota Bakken shale. When the relative displacement of the fracture faces reaches the threshold value δ_0 (cohesive crack tip), the cohesive strength $\tau_{\max}$ is reached and the faces of the cohesive element starts to separate. Total failure is reached at the material crack tip δ_f, where cohesive stress decreases to zero. The bilinear CZM depends on the initial stiffness K_0, the cohesive strength $\tau_{\max}$ and the failure displacement δ_f, which can be equivalently represented by the cohesive energy release rate G_{IIc}, is defined as

$$G_{IIc} = \int_0^{\delta_f} \tau \mathrm{d}\delta \tag{7}$$

3.2. Requirements on the Cohesive Stiffness

The stiffness of a cohesive element with zero thickness should ensure that in the elastic domain, a material represented by a bulk material with embedded cohesive zones has the same stiffness as the bulk material alone (**Turon et al., 2007**). Figure 3 shows how cohesive elements affect the deformation of such a sandwich composite. Assuming a uniform distribution of strain and stress, we have

$$\tau = G\gamma = K_0\Delta; \quad \gamma_e = \delta + \Delta/2t \tag{8}$$

The equilibrium condition $\tau_e = \tau = G_e\gamma_e$ requires that the effective shear modulus satisfy:

$$G_e = G(1/1+G/2K_0t) \tag{9}$$

Because the cohesive stiffness should not affect the effective modulus, thus, $G \ll 2K_0t$. We note: $K_0 = \beta G/t$. Usually a very large value of β is used, as long as simulations do not exhibit any oscillations.

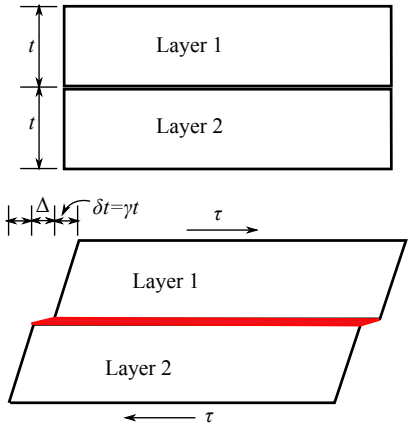

Fig. 3. Influence of the stiffness of a cohesive zone in a numerical model of laminated material.

3.3. Calibration of the Cohesive Strength

The cohesive strength is different from the yield strength that corresponds to damage initiation or the peak stress during triaxial compression test. By contrast, cohesive strength refers here to the critical point at which micro-crack propagation in the damaged zone cannot be

predicted by a continuum-based approach: after this critical point, micro-cracks developed within the Representative Volume Element (RVE) interact with each other. In order to capture the transition between the propagation of a smeared damaged zone and the propagation of a discrete fracture, we calculate the damaged shear modulus of a 2D REV that contains one set of parallel equally sized cracks, using two methods: first, the DSID model, which does not account for micro-crack interaction; second, **Kachanov (1992)** micro-mechanical model, which accounts for micro-crack interaction.

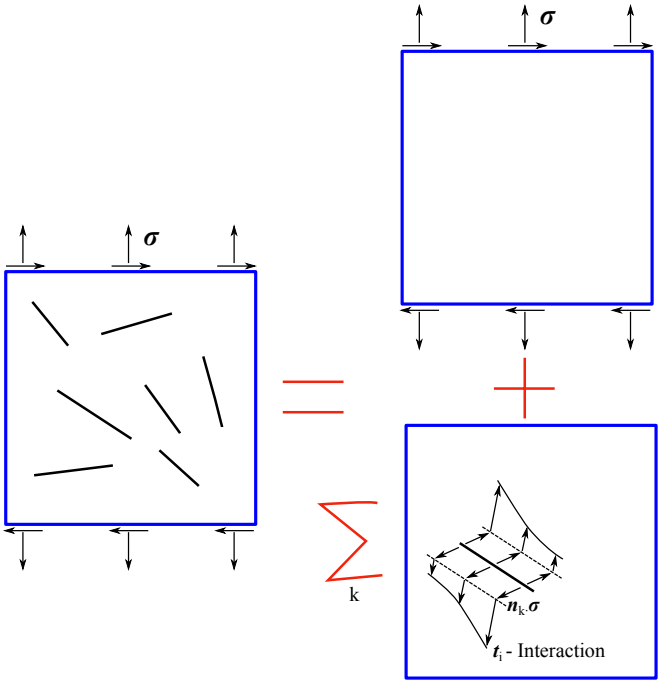

Fig. 4. Fundamental assumptions of Kachanov's micromechanical model

In the 2D micromechanical damage model, the effective strain of a linear elastic REV containing N cracks subjected to the far field stress σ^{∞} is calculated as the sum of the strain produced by σ^{∞} and the strain induced by the displacement jumps at crack faces, which are subjected to local tractions $t_i^0 = n_i \cdot \sigma^{\infty}$. The problem is solved by superposition as illustrated in Figure 4: N independent plates are considered, in which the ith crack is subjected to the traction t_i^0 due to the field stress and additional tractions due to crack interaction. The total traction t_i on each crack face can be calculated by solving a system of integral equations as

$$t_i(\zeta_i) = t_i^0 + n_i \cdot \sum_{j \neq i} \int_{-l_j}^{l_j} \sigma_j^n(\zeta_i, \zeta_j) \left[n_j \cdot t_j(\zeta_j) \right] d\zeta_i + n_i \cdot \sum_{j \neq i} \int_{-l_j}^{l_j} \sigma_j^{\tau}(\zeta_i, \zeta_j) \left[\tau_j \cdot t_j(\zeta_j) \right] d\zeta_i \tag{10}$$

In which l_j is the half-length of the jth crack, τ_j is the unit vector, which is tangential to the face of the jth crack. $\sigma_j^n(\zeta_i, \zeta_j)$ (respectively $\sigma_j^{\tau}(\zeta_i, \zeta_j)$) is the stress tensor at point ζ_i of the i th crack, generated by a pair of equal and opposite unit forces located at point ζ_j along the normal (respectively tangential) direction of the jth crack. We assume that the stress at ζ_j is not sensitive to the deviation of $t_j(\zeta_j)$ from its average $\langle t_j \rangle$, thus, Eq.10 can be formulated in terms of average tractions applied to each crack considering far field stress and interaction effect. Once the average tractions on each crack face $\langle t_i \rangle$ is obtained, the average relative displacement vector $\langle b_i \rangle$ across the faces of ith crack is determined by superposing the displacements due to punctual tractions at each point of the ith crack faces:

$$\begin{aligned} \langle b_i \rangle &= \frac{4 l_i}{E_0} \int_{-l_i}^{l_i} t_i(\zeta_i) \left[1 - \left(\zeta_i / l_i \right)^2 \right]^{1/2} \mathrm{d}\zeta_i \\ &= \pi l_i \langle t_i \rangle / E_0 \end{aligned} \tag{11}$$

Where E_0 is the Young's modulus of the matrix. The average strain of the studied REV with area A is calculated as

$$\begin{aligned} \langle \varepsilon \rangle &= \mathbb{S}_{\text{eff}} : \sigma^{\infty} \\ &= \mathbb{S}^0 : \sigma^{\infty} + \frac{l_i}{2A} \sum_{i=1}^{N} \left[n_i \otimes \langle b_i \rangle + \langle b_i \rangle \otimes n_i \right] \end{aligned} \tag{12}$$

In which $\mathbb{S}^0$ and $\mathbb{S}_{\text{eff}}$ are the fourth order reference and effective compliance tensors. The effective Yong's modulus or shear modulus are determined by combining Eq.10-12.

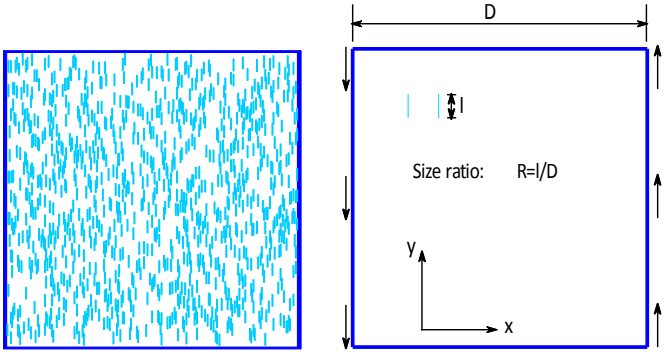

Fig. 5. Random crack patterns generated to calculate the damaged shear modulus according to Kachanov's micro-mechanics model

In the following, we consider a 2D REV that contains cracks perpendicular to the x-axis (Figure 5), and we calculate the effective shear modulus in the xy-direction. We generated a crack pattern in which centers were randomly distributed, with a targeted crack density defined as

$$\rho = \frac{1}{A}\sum_{i=1}^{N} l_i^2 \tag{13}$$

Where A, l_i and N are respectively the area of REV, the half-length of i th crack and the number of cracks. Note: we ensured that cracks did not intersect each other, and that the size ratio of crack over REV should not exceed a certain value (in order to ensure REV requirements). Because all the cracks considered were perpendicular to the x-axis, the effective modulus is affected by crack density ρ in Kachanov's model, and by the xx-component of the damage tensor (Ω_x) in the DSID model. We simulated a simple shear test and used Eq.12 to obtain the effective shear modulus for several values of crack density, which we varied by either increasing the number of cracks in the REV with a fixed crack length (crack initiation), or by increasing the length of a fixed number of cracks in the REV (crack propagation). Similarly, we calculated the reduction of effective shear modulus with increasing damage component Ω_x at the material point according to the DSID model:

$$\mathbb{S} = \partial^2 G_s / \partial \sigma^2 \tag{14}$$

Where G_s is Gibbs energy defined in Eq.1.

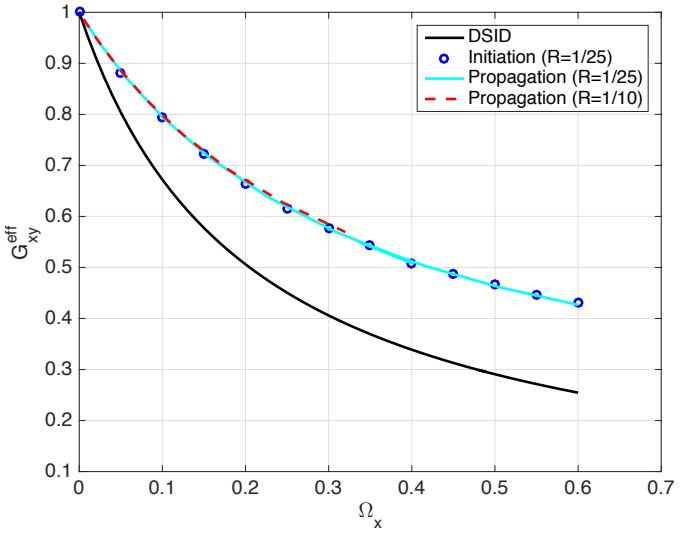

Fig. 6. Damaged shear modulus calculated with the DSID model and with Kachanov's micro- mechanical model for a set of cracks parallel to the y-axis. Damage propagation is modeled by increasing the length of a fixed number of equally sized cracks, and damage initiation is modeled by increasing the number of cracks with fixed sized.

For the calibrated parameters listed in Table 1, the shear modulus reduction curve predicted by the DSID model is shown in Figure 6 (solid black). As for the micromechanical model, the modulus decreases when damage increases, but the tangent to the modulus/damage curve has a lower value than for the DSID model. This is because the micromechanical model accounts for the shielding effect due to crack interactions. Figure 6 also shows that the value of damaged elastic moduli only depends on crack density and not on the type of damage growth (crack initiation vs. crack propagation). We note that the relative difference between effective shear modulus predicted by DSID and by Kachanov's method keeps constant after Ω_x or $\rho = 0.3$. Because the rate of shear modulus degradation is mainly controlled by the interaction or non-interaction between cracks, we consider that Ω_x =0.3 is the critical damage value in mode II, which marks the transition between continuum damage and discrete fracture.

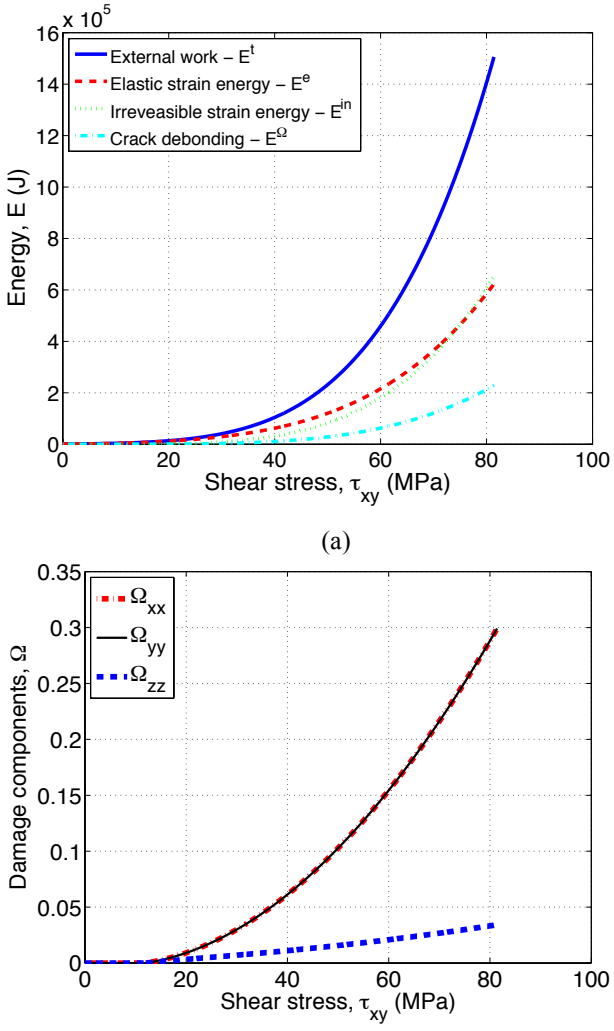

Fig. 7. Material Point simulation of a confined shear test (pure mode II) with the DSID model, up to the critical damage value: energy components evolution (a) and damage growth (b).

We simulated a confined shear test at the material point, with the DSID model. Following loading paths adopted in the laboratory experiments performed by ConocoPhillips, we applied a 6.9 MPa hydrostatic confining pressure before applying the shear stress. According to our transition model, we stopped the simulation when damage in the direction perpendicular to the shear direction reached 30%. From the simulation shown in Figure 7, we found that the corresponding shear stress was τ_{max} =81.4 MPa.

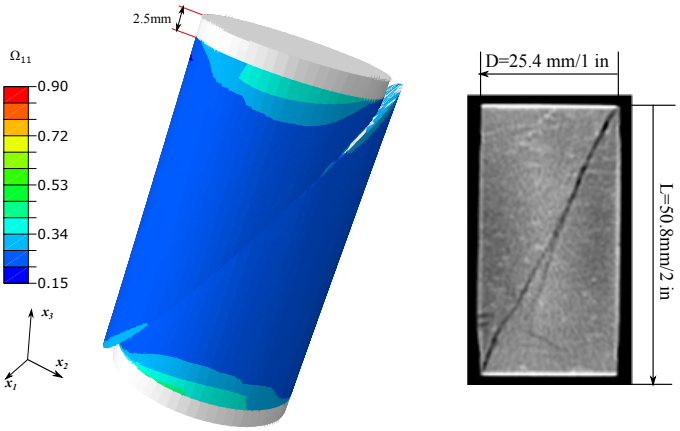

Fig. 8. Damage distribution along the horizontal direction for a triaxial compression test (left) and typical shear failure plane observed in shale after triaxial compression (right).

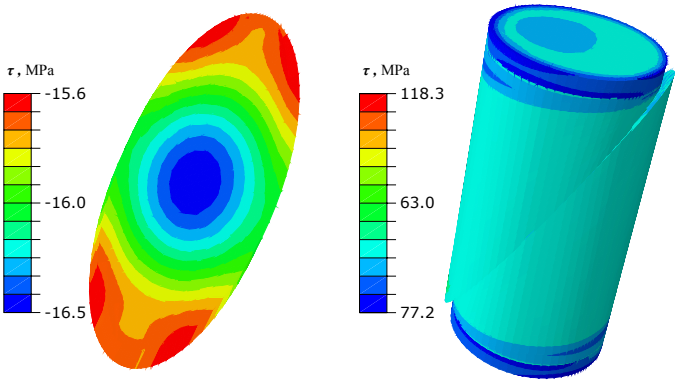

Fig. 9. Shear stress distribution along the long axis of an ellipse within the cohesive zone layer after the initiation of debonding and before the total failure (left) and Tresca stress distribution for the whole cylinder just after failure (right) subsequent to a triaxial compression test.

3.4. *Calibration of the Cohesive Energy Release Rate*

As shown in Figure 2, the bilinear cohesive zone model requires a third parameter in addition to the CZM stiffness and CZM shear strength: either the relative displacement at failure or the cohesive energy release rate. Mechanically, cohesive elements and their surrounding elements start to unload once the cohesive strength is reached. Then, the elastic energy stored within surrounding (bulk) elements flows into a cohesive segment and is dissipated to create new surfaces. The determination of the exact amount of energy that flows into cohesive elements would require additional laboratory measures. In this paper, we calibrated the value of the cohesive energy release rate G_{IIc} against the energy released during a confined triaxial compression test conducted in ConocoPhillips rock mechanics laboratory. In order to predict the propagation of damage followed by shear failure numerically, and to reproduce the typical shear failure plane observed in shale after triaxial compression tests (Figure 8), we constructed a Finite Element model of shale plug with the exact same dimensions as in the experiments. We modeled a plane of weakness along the diagonal of cylinder with a single 2D planar cohesive zone. We used a cohesive stiffness of $K_0 = 50G_0$ and a cohesive shear strength of τ_{max} =81.4 MPa. The bulk of the material was modeled with the DSID model with the parameters calibrated in Section 2. In lab experiments, friction between the sample and the steel loading plates has a significant influence on the global stress-strain behavior. Thus, we considered that the elements representing the plates and those that represented elements of rock in contact with the platens shared the same nodes. The thickness of the plates in the simulation was 2.5 mm. Steel plates were assigned linear elastic behavior, with a Young's modulus of E=200 GPa and a Poisson's ratio of ν=0.3.

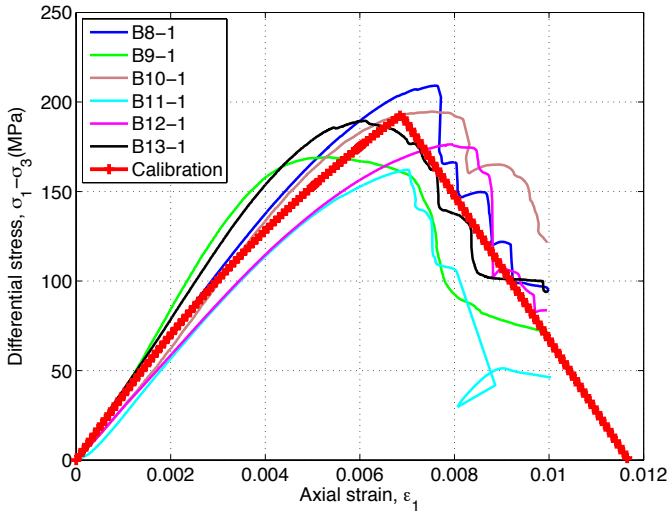

Fig. 10. Experimental and numerical stress/strain curves obtained during triaxial tests with σ_3=6.9 MPa. Note: samples B8-B13 correspond to different lithologies, which have different stress/strain curves.

During the simulation, we fixed the 6 degrees of freedom of the center point in the bottom steel plate to prevent free body movement, and constrain the axial displacement of the bottom plate. During the first stage of the simulation, we applied the confining pressure σ_3 =6.9 MPa around the sample (except the bottom steel face). Then we applied an axial displacement boundary

condition at the top face of the top steel plate. This sequence reproduces exactly the procedure employed in the lab experiments. Figure 8 gives the vertical crack distribution perpendicular to x_1 axis (damage along x_1) of the simulated cylinder when complete failure happens, i.e. total displacement was 0.708 mm. Except for the boundary in contact with the steel plate, the value of horizontal damage was uniformly distributed. Note that displacements were magnified 5 times in all figures. Figure 9 shows the Tresca effective stress distribution in the cylindrical sample and the shear stress along the shear direction inside the cohesive layer right before the total failure, when the vertical displacement of the top steel plate was 0.652 mm. We note similar boundary effects close to the edge of the plate and everywhere else, a uniform effective stress distribution. All the elements inside the cohesive layer entered the softening regime at this stage, and captured failure localization with macro shear fracture initiation close to the steel plates as observed in the experiments.

After the simulation, we extracted the mean axial stress and the average displacement at the top steel plate. The differential stress was obtained by subtracting the confinement 6.9 MPa out of the mean stress, and the axial strain was obtained by dividing the mean displacement by the sample length and by subtracting the strain due to confining pressure. Figure 10 compares the stress/strain curves obtained in the lab to those obtained during the simulations. Because the model of stiffness reduction with damage was calibrated against pre-peak points of the stress/strain curve, it is clear that the peak stress is well captured in the simulations. As explained above, the cohesive shear energy release rate was calibrated by trial and error to match the softening regime of stress-strain curve. For the set of lab results used in this study, we obtain an average of G_{IIc}=25 KJ, which is satisfactory for shales that exhibit some lithological variation.

4. MULTISCALE FRACTURE PROPAGATION WITH NO PREASSIGNED PATH

4.1. Fracture Path Set up

The most successful numerical tools for modeling fracture propagation are cohesive zone elements and XFEM. Compared to XFEM, the major drawback of CZM is that pre-assigned fracture paths are needed, which is challenging because fracture paths are vastly unknown for complicated geometry and boundary conditions. To overcome this shortcoming, we propose to insert cohesive elements around all the Finite Elements that represent the bulk (DSID elements), so that the edges of each element become potential fracture paths. Coupling a high number of cohesive elements with DSID elements works perfectly well when the local stress in each cohesive segment is tensile shearing. However, when compressive shearing happens, Finite Elements along the cohesive segment sometimes overlap with each other, which stops the simulation. Additional contact properties need to be added to the element edges to ensure convergence. In this paper, we introduce a non-penetration condition at the contact of two neighboring surfaces of the same cohesive element. These two surfaces are defined frictionless because their shear behavior is governed by the Mode II cohesive law of the cohesive element. Generating such contact laws in addition to CZM elements at the edges of all elements is impossible to do with the Abaqus CAE user interface. Therefore we wrote a dedicated Python program to generate the desired input file.

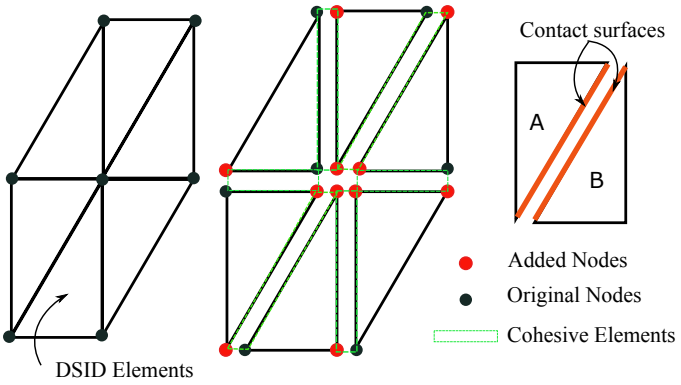

Fig. 11. Sketch of the process adopted in Python to add cohesive elements and contact properties to all Finite Elements.

Figure 11 shows the procedure adopted in the Python program to generate the input file. In summary:

- Construct the geometry of simulation model, assign the corresponding material, and mesh the domain with triangular elements to generate the complete input file without cohesive elements. (Note: we chose triangular elements to allow shear facture propagation)
- In Python program, read the coordinates of all the nodes, the connectivity tables of all element types and read the numbers of the elements, nodes and surfaces subjected to boundary conditions from the generated input file.
- Loop through the connectivity table to find the elements sharing two nodes (2D). Find the corresponding edges sharing nodes by matching global nodes to local nodes. Pairs of surfaces for CZs are defined on elements that share the same edges (identified by their numbers). Store those elements numbers and their local edge numbers.
- Loop through all elements, if the current element shares the same node with another element from the connectivity table, add another node with the

same coordinates, and replace global node number with the added node number for the second element.

- Loop through all elements with updated connectivity table, comparing the coordinates of each node for current element and another element, if the two elements have two pair of two nodes with same coordinates, use the four nodes to construct a cohesive element. (Note: the order of the four node numbers needs to follow the local numbering sequence). Store the new connectivity table for all the cohesive elements.
- For each node set with displacement boundary conditions, compare the coordinates of each node in that set with all added nodes: if they have the same coordinates, add the node to this node set. (This procedure ensures the displacements are the same for all nodes with same coordinates)
- Write out all nodes, connectivity tables, node sets, element sets and surface sets to the new input file following the structure of Abaqus input file rules.

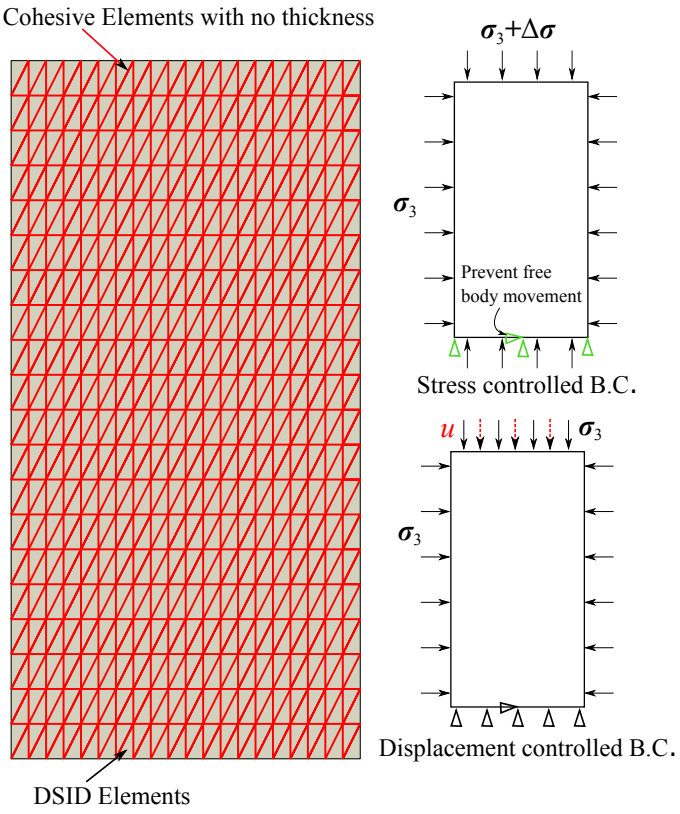

Fig. 12. DSID (grey triangle)/cohesive (highlighted in red) element mesh set up and boundary conditions adopted to simulate multi-scale fracture propagation in shale. Note that in the stress-controlled case, the displacement constraint at the bottom boundary is to ensure no rigid body movement.

4.2. Numerical Simulation

In the previous sections, we showed how the parameters for both the DSID model and the CZM can be calibrated by using laboratory rock mechanics experiments and three-dimensional simulations. In the following section, we use our coupled DSID/CZM model to simulate an idealized 2D biaxial compression test in which all DSID elements are surrounded with cohesive elements, as shown in Figure 12. Macro fracture can develop and propagate anywhere along DSID element boundaries.

We used structured plane strain triangle elements to mesh the whole domain. With the proposed Python program, we inserted CZMs at the edges of triangular DSID elements and added contact properties to the new surfaces. The constitutive parameters of DSID used in this simulation are listed in Table 1, the cohesive shear strength was $\tau_{\max}$=81.4 MPa and the cohesive energy release rate was G_{IIc}=25 KJ. We used a cohesive stiffness of $K_0 = 150G_0$ to ensure that the presence of a great number of cohesive elements has negligible influence on the behavior of shale prior to macro fracture propagation. Because the shear strength we calibrated is obtained from material point simulations with a confining pressure σ_3=6.9 MPa, we applied a 6.9 MPa confinement stress at all external boundaries of the domain in the stress controlled case (Figure 12), and to all boundaries except the bottom boundary (subjected to vertical displacement constraints) in the displacement controlled case. Note that in addition, we imposed displacement constraints at the bottom boundary, as follows: fixed vertical displacement at the left and right bottom vertex points, fixed vertical and horizontal displacements at the middle point (Figure 12). This is to ensure no free body movement. In the second sequence, we applied an additional vertical stress $\Delta\sigma$ at the top and bottom boundaries of the domain in the stress controlled case, and an additional displacement u at the top boundary in the displacement controlled case.

Figure 13 shows the horizontal damage Ω_x (vertical micro crack) distribution inside the DSID elements and cohesive zone damage D (facture) distribution inside the cohesive element for stress controlled simulation when applied additional stress $\Delta\sigma$=201 MPa. The cohesive damage D is defined as

$$D = \frac{\delta - \delta_0}{\delta_f - \delta_0} \tag{15}$$

Note δ is the current shearing displacement jump and the displacement field is magnified 5 times. When D reaches 1, complete failure happens. We can see that shear failure develops along the diagonal of the simulation domain and the micro vertical crack concentrate along macro fracture.

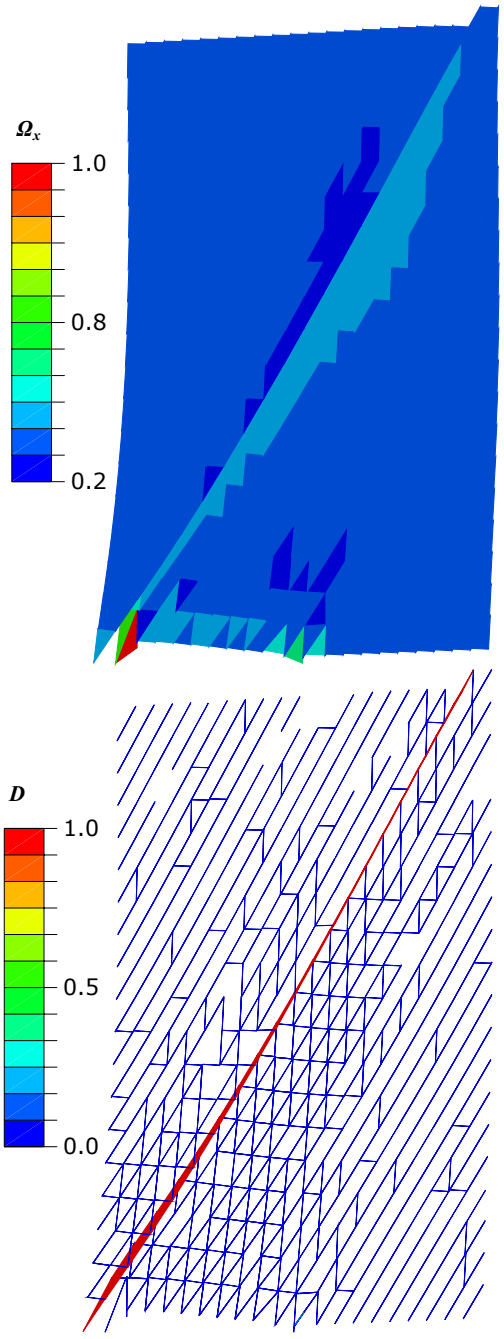

Fig. 13. Horizontal damage Ω_x (vertical micro crack) distribution (top) and cohesive zone damage D (macro fracture) distribution for stress controlled simulation when applied additional stress $\Delta\sigma$ =201 MPa.

Figure 14 shows the horizontal damage Ω_x (vertical micro cracks) distribution inside the DSID elements and the cohesive zone damage D (facture) distribution inside the cohesive element for the displacement controlled simulation when the imposed vertical displacement is u =0.685 mm. Note the simulation stopped before total failure was reached. We magnified displacements 10 times to highlight macro fracture patterns. We note that the displacement-controlled test yields several fractures, and that micro cracks concentrate along those fractures. These phenomena illustrate the transition from micro crack to macro fracture theory. The two sets of boundary conditions produce completely different damage distributions and macro fracture patterns.

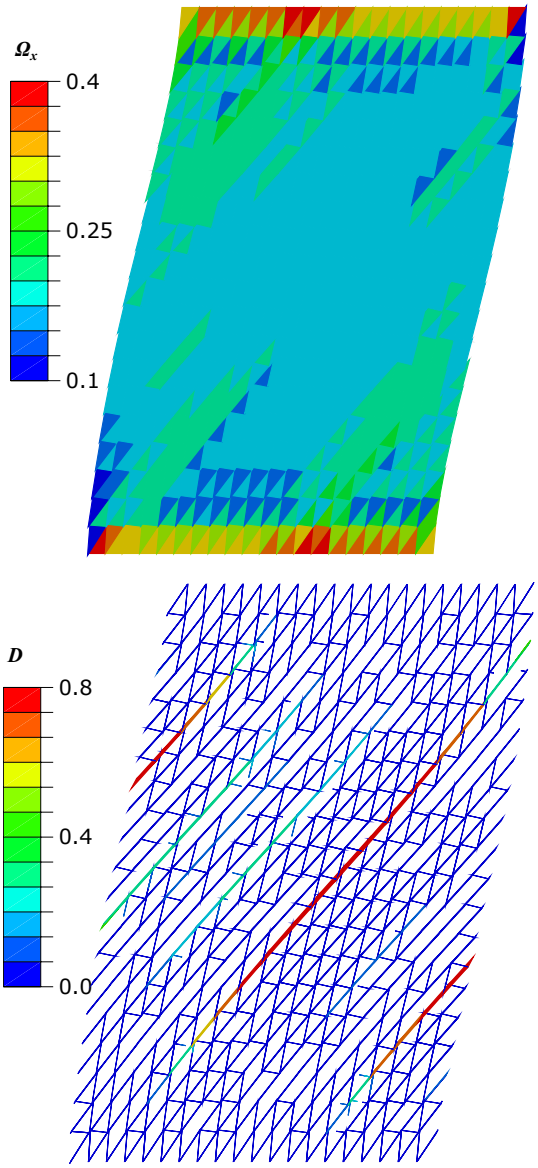

Fig. 14. Horizontal damage Ω_x (vertical micro crack) distribution (top) and cohesive zone damage D (macro fracture) distribution for displacement controlled simulation when the applied vertical displacement is u =0.685 mm.

We extracted damage induced inelastic strain energy at each Gauss point and multiplied it with the total volume in order to calculate the total dissipated energy due to micro crack development $E_{id} = \int \sigma : \epsilon^{id} dV$. We compared it with the total cohesive energy $E_c = \int_S \sigma : \delta \mathrm{d}S$ dissipated to create new material surfaces (Figure 15). In both tests, a great amount of energy is dissipated for micro crack development before macro cohesive fracture starts propagating. The response of the material in the stress-controlled test is brittle, with rapid fracture propagation. In the displacement-

controlled test, additional micro crack development is needed to trigger total failure.

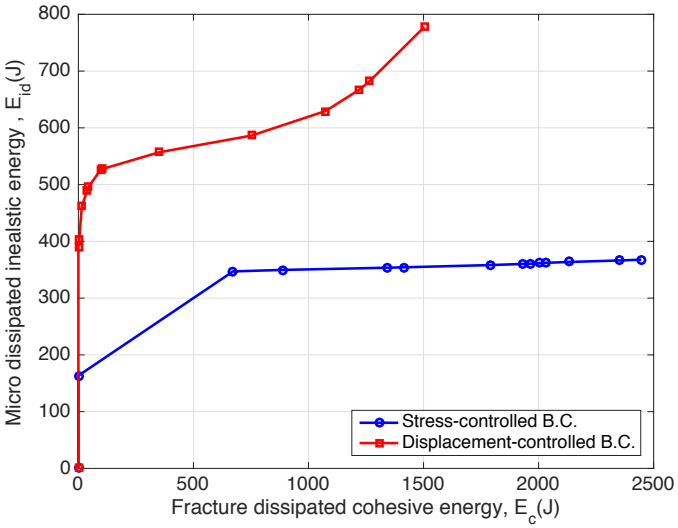

Fig. 15. Comparison of the forms of energy dissipated during simulation: energy released by the creation of new material surfaces in the cohesive zone and energy dissipated by continuum damage propagation. Note: the energy dissipated by cohesive elements amounts to 25kJ (calibrated value above) only if the final fractured surface reaches 1 m^2. Here, the energy dissipated at total failure is less because the area of the open fracture is less than 1 m^2.

5. CONCLUSION

We proposed a strategy to couple micro-crack propagation to unconstrained fracture pattern formation in mode II failure. In the numerical model, macro-scale fractures were represented by Cohesive Zones defined at the boundaries of all the Finite Elements, which were assigned a continuum anisotropic damage model – the DSID model. DSID parameters of the continuum anisotropic damage model were calibrated against triaxial compression tests performed on Bakken shale. We compared the reduction of shear modulus with damage predicted by DSID, which does not account for crack interaction, with that predicted by Kachanov's micromechanical model, which accounts for crack interaction. The results show that the critical damage threshold, at which crack interaction cannot be neglected, is equal to 0.3. We employed this critical value to calibrate the cohesive strength of the Cohesive Zone Model (CZM). The energy release rate of the CZM was calculated by matching simulation results with the post-peak stress-strain curves obtained experimentally during triaxial compression tests. We used our CZM-DSID model to simulate a biaxial compression test in plane strain. In stress-controlled conditions, the shale sample exhibits a brittle response with rapid macro-fracture propagation along a line parallel to the direction of maximum shear stress. In displacement-controlled conditions, micro-crack propagation is less localized, macro-fractures initiate at several locations in the sample, and failure is not reached. In both cases, simulation results illustrate the transition from accumulated micro damage to macro fracture propagation. These encouraging results open new perspectives for the simulation of multi-scale fracture propagation and the fundamental understanding of the interactions between fracture tip advancement, friction at the fracture faces, and micro-crack propagation along fractures. The mesh chosen in the simulations constrains the fracture path. This topological constraint can be relaxed by refining the mesh and assigning a cohesive zone at each element boundary. Future work will be dedicated to the level of mesh refinement necessary to predict a mesh-independent fracture path.

ACKOWLEGEMENTS

Financial support for this research was provided by ConocoPhillips and by the Offices of the Executive Vice President for Research and the Provost – Georgia Tech Fund for Innovation in Research and Education.

REFERENCES

1. Mazars J. and G. Pijaudier-Cabot. 1996. From damage to fracture mechanics and conversely: a combined approach. *Int. J. Solids Struc.* 33(20):3327–3342.
2. Xu X.P. and A. Needleman. 1994. Numerical simulation of fast crack growth in brittle solids. *J. Mech. Phys. Solids* 42:1397–1434.
3. Comi C., S. Mariani and U. Perego. 2007. An extended fe strategy for transition from continuum damage to mode I cohesive crack propagation. *Int. J. Numer. Anal. Methods Geomech.* 31(2):213.
4. Jirasek M. and T. Zimmermann. 2001. Embedded crack model: I. basic formulation. *Int. J. Numer. Methods Eng.* 50(6):1269–1290.
5. Cuvilliez S., F. Feyel, E. Lorentz and S. Michel-Ponnelle. 2012. A finite element approach coupling a continuous gradient damage model and a cohesive zone model within the framework of quasi-brittle failure. Comput. *Method Appl. M.* 237:244–259.
6. Xu H. and C. Arson. 2015. Mechanistic analysis of rock damage anisotropy and rotation around circular cavities. *Rock Mech. Rock Eng.* :1–17.
7. Amendt D., S. Busetti and Q. Wenning Q. 2013. Mechanical characterization in unconventional reservoirs: a facies-based methodology. *Petrophysics* 54(05):457–464.
8. Turon A., C.G. Davila, P.P. Camanho and J. Costa. An engineering solution for mesh size effects in the simulation of delamination using cohesive zone models. *Eng. Fract. Mech.* 74(10):1665–1682.
9. Kachanov M. 1992. Effective elastic properties of cracked solids: critical review of some basic concepts. *Appl. Mech. Res.* 1992; 45(8):304–335.